

Assessment of algebraic subgrid scale models for the flow over a triangular cylinder at $Re = 45000$

D.A. Lysenko^{a,*}, I.S. Ertesvåg^b

^a3DMsimtek AS, 88, NO-4056 Tananger, Norway

^bDepartment of Energy and Process Engineering, NTNU Norwegian University of Science and Technology, Kolbjørn Hejes vei 1B, NO-7491, Trondheim, Norway

ARTICLE INFO

Keywords:

triangular cylinder
large-eddy simulation
algebraic subgrid scale models
turbulent separated flows
OpenFoam
CFD

ABSTRACT

The turbulent separated flow over an equilateral triangular cylinder at a Reynolds number 45000 (based on the triangle edge) is studied by means of large-eddy simulation (LES). The moderate Reynolds number is chosen in order to replicate available experimental data (Laser Doppler Anemometry measurements at the Volvo test rig). The OpenFoam CFD toolbox is used for the present numerical simulations. Several algebraic subgrid scale (SGS) closures, including the conventional Smagorinsky model ($C_s = 0.1$ and $C_s = 0.053$), the model by Vreman ($C_s = 0.1$) and the dynamic version of the k -equation model are investigated. The spectral analysis of the vortex shedding and the convective instabilities as well as the turbulence kinetic energy dissipation rate is presented. Some aspects of the blockage effects are investigated and compared to experimental data available in the literature. It was shown that blockage affects significantly the mean drag and pressure coefficients of the triangular cylinder. At the same time the mean velocity field is tending to similarity. Overall, all SGS models reproduced most important aspects of the flow physics of the separated bluff-body flow, including integral flow parameters and spectral characteristics with dispersion about 10%, showing a reasonable consistency with the experimental data.


1. Introduction

Turbulent, separated bluff-body flows are implicated in a wide range of engineering applications. However, in spite of the fact that the flow physics has been investigated intensively by both numerical and experimental methods during the last century (the first viscous flow past a circular cylinder probably was obtained by Thom [45] in 1933), accurate simulations are of great practical importance still.

The aim of the present work is to develop a large-eddy simulation model (LES) of the turbulent, separated bluff-body flows at high Reynolds numbers, interesting for many practical applications. The present LES is based on the core numerical method implemented in the OpenFoam toolbox [51], which became very popular in industrial engineering and academic research during the last decade. Previously, several systematic studies have been performed to validate and verify the OpenFoam capabilities for several turbulent bluff-body flows at the moderate Reynolds numbers, $Re = 3900 - 50000$ [22],[24],[21]. Here, the Reynolds number is defined as $Re = \rho_\infty U_\infty H / \mu$, where U_∞ and ρ_∞ are the free-stream velocity and mass density, respectively, H is the diameter of the obstacle and μ represents the dynamic viscosity. These works presented results both the conventional approach for solution of the unsteady, compressible Reynolds-averaged Navier-Stokes equations (URANS)[23] and an advanced LES technique [22],[24]. Lately, both inert and reactive flows over a triangular cylinder at $Re \approx 50000$ using unsteady Reynolds-averaged Navier-Stokes (URANS), LES and Scale-Adaptive simulations (SAS) have been investigated [21]. The global descriptions of LES, SAS and RANS/URANS indicated a clear interrelation between these three approaches to simulation of the turbulent (combustion) flows [21]. In general, reasonable consistency was found for these different approaches as well as satisfactory agreement between numerical simulations and measurements. However, the most accurate results were reached using the large-eddy simulations.

Scientific and engineering background to investigate triangular cylinders is commonly driven by aerospace industry, in particular, propulsion and industrial combustion systems, where bluff-body wakes are used for the flame stabilization. Also, the simplicity of configuration is quite attractive to provide fundamental research of turbulent combustion

*Corresponding author

 dmitry.lysenko@3dmsimtek.no (D.A. Lysenko); ivar.s.ertesvag@ntnu.no (I.S. Ertesvåg)

ORCID(s): 0000-0001-7511-2910 (D.A. Lysenko)

as well as computational test cases [41]. Another common applications are flow metering, where triangular cylinders are commonly used as a vortex shedder in the vortex-type flow meters [53].

The triangular cylinder was extensively investigated experimentally and numerically in the literature [3], [32], [11], [44], [42], [39], [31], [57], [53]. Among them, two experimental works can be highlighted, which provided the local flow characteristics, suitable for the detail validation of large-eddy simulations. Calvert [3] presented Hot-Wire Anemometry (HWA) measurements of the bluff-body wake at the blockage ratio, $BR = 1/10$. Sjunnesson et al. [42] provided Laser Doppler Anemometry (LDV) measurements of the wake at $BR = 1/3$. However, both studies missed the key flow parameters like forces coefficients. Yagmur et al. [53] investigated the triangular cylinder both by means of Particle Image Velocimetry (PIV) and LES for the highest Reynolds number, $Re = 11600$. Dynamics of the wake (in terms of Strouhal number) was investigated extensively as well by many researchers, however, experimental results for the local dynamics of the separated shear layers are not available yet. It is worth to notice, that important information related to the key integral flow features like the lift, drag and pressure forces is limited. Okamoto et al. [32] and Tatsuno et al. [44] presented the drag coefficient for the Reynolds number, $Re = 22000$ and $Re = 90000$, respectively. Yagmur et al. [53] reported the drag using LES for [53]. The alternative measured data of the drag force can be found in NACA TN3038.

The present study we investigated the turbulent flow over triangular cylinder at different configurations ($BR = 1/3$ and $BR = 1/9, 1/20$) to replicate the experimental data by Calvert [3] and Sjunnesson et al. [42] and investigate the blockage effects. The lift, drag and pressure coefficients are reported and compared with the available data as well. An assessment of the several subgrid scale (SGS) models for the turbulent flow over an equilateral triangular cylinder is provided. The conventional Smagorinsky model [43] with two constants ($C_s = 0.1$ and $C_s = 0.053$), the Vreman model ($C_s = 0.1$) [49] and the dynamic version of the k -equation eddy-viscosity model [55] are investigated. Some numerical aspects, like the spectral analysis of the convective instability of the separated shear layers and the turbulence energy dissipation, missed in our previous study [21], are reported. The Volvo test rig has been chosen due to the available LDV measurements of the velocity [42].

In the present work we utilized the standard numerical platform (the second-order finite-volume method) implemented in the OpenFoam code. This numerical approach has been validated in details for the bluff-body flows during the last decade (e.g., [22], [24], [4], [37], [5], [21], [56]) and can be recommended to simulate the turbulent separated flows.

The paper is divided into five main sections. The first section of the paper describes the mathematical modeling and numerical aspects. Then, a general description of the test case is given. Finally, computational results are presented, results are analyzed and discussed, and on the top of that conclusions are drawn.

2. Brief description of mathematical modeling numerical aspects

In order to be consistent with authors' previous results [22], [24], [21], the compressible flow and related numerical setup were considered despite of the fact that the actual Mach number was close to the incompressible limit.

2.1. Mathematical modeling

The Favre filtered balance equations of mass, momentum and energy were solved. In the present work, the Mach number was set to a quite small value, $M = U_\infty/c_\infty = 0.05$, assuming the subgrid scales incompressibility hypothesis. Here, c_∞ is the speed of sound in the free stream.

The subgrid scale models are important for any large-eddy simulation in research of the turbulent separated flows. The algebraic type of eddy-viscosity SGS models are quite popular in the state-of-the-art codes due to their robustness and principal property to possess the dissipative nature of turbulence [49]. In the present study we have investigated several of them.

2.1.1. The k -equation model

As it was mentioned by Chaouat [7], the modeling of the subgrid energy equation has been worked out by several authors, such as Schumann [40], Horiuti [15] and Yoshizawa [55], inspired by analogy from its corresponding Reynolds-averaged Navier-Stokes modeling.

The k -equation eddy viscosity subgrid scale model [55] (hereafter dTKE) is based on the SGS kinetic energy $\tilde{k} = \frac{1}{2} (\overline{\mathbf{u} \cdot \mathbf{u}} - \tilde{\mathbf{u}} \cdot \tilde{\mathbf{u}})$, where $\tilde{\mathbf{u}}$ is the density weighted filtered velocity. The following assumptions for the SGS

density weighted stress tensor \mathbf{B} and the filtered deviatoric part of the rate of strain tensor $\tilde{\mathbf{D}}_D$ were used:

$$\mathbf{B} = \frac{2}{3}\bar{\rho}\tilde{k}\mathbf{I} - 2\mu_B\tilde{\mathbf{D}}_D, \quad (1)$$

$$\tilde{\mathbf{D}}_D = \left[\tilde{\mathbf{D}} - \frac{1}{3}(\text{tr } \tilde{\mathbf{D}})\mathbf{I} \right], \quad (2)$$

$$\tilde{\mathbf{D}} = \frac{1}{2}(\text{grad } \tilde{\mathbf{u}} + \text{grad } \tilde{\mathbf{u}}^T), \quad (3)$$

$$\mu_B = c_k\bar{\rho}\sqrt{\tilde{k}}\Delta. \quad (4)$$

Here \mathbf{I} is the unit tensor, $\bar{\rho}$ the filtered density, μ_B the SGS viscosity and Δ the top-hat filter with a length estimated as the cubic root of the control volume. The subgrid kinetic energy \tilde{k} was estimated by solving a separately modeled transport equation of the form,

$$\frac{\partial \bar{\rho}\tilde{k}}{\partial t} + \frac{\partial \bar{\rho}\tilde{k}\tilde{u}_j}{\partial x_j} = F_p + F_d - F_e, \quad (5)$$

$$F_p = -\mathbf{B} \cdot \tilde{\mathbf{D}}, \quad (6)$$

$$F_d = \frac{\partial}{\partial x_j} \left((\mu_B + \mu) \frac{\partial \tilde{k}}{\partial x_j} \right), \quad (7)$$

$$F_e = c_e \bar{\rho} \tilde{k}^{3/2} / \Delta, \quad (8)$$

where F_p is production, F_d diffusion and F_e dissipation terms, respectively, and $c_k = 0.07$, $c_e = 1.048$ are model coefficients [38].

The dynamic model for the k equation can be derived using the Germano identity \mathbf{L} with another filter kernel of width $\bar{\Delta} = 2\Delta$. The theoretical background and implementation details are provided by Fureby [12].

2.1.2. The Smagorinsky model

The conventional Smagorinsky SGS model (hereafter SMAG) can be recovered from Eq. 5 by assuming local equilibrium, i.e., $F_p = F_e$. Thus, the SGS kinetic energy can be computed from the relation

$$\mathbf{B} \cdot \tilde{\mathbf{D}} + c_e \bar{\rho} \tilde{k}^{3/2} / \Delta = 0. \quad (9)$$

Using Eq. (1) and introducing the following coefficients,

$$a = \frac{c_e}{\Delta}, \quad b = \frac{2}{3}\text{tr } \tilde{\mathbf{D}}, \quad c = -2c_k\Delta\tilde{\mathbf{D}}_D \cdot \tilde{\mathbf{D}}, \quad (10)$$

the relation of Eq. (9) can be reformulated to a quadratic equation for $\sqrt{\tilde{k}}$. The final relation for \tilde{k} can be formulated as

$$\tilde{k} = \left(\frac{-b + \sqrt{b^2 - 4ac}}{2a} \right)^2 \quad (11)$$

The models constants are: $c_k = 0.02$ and $c_e = 1.048$ [38]. The dissipation rate $\tilde{\epsilon}_{\text{sgs}}$ from the SMAG model was expressed according to Eq. 8.

2.1.3. The Vreman model

Vreman [49] proposed to express the eddy viscosity as

$$\mu_B = c_v \bar{\rho} \sqrt{\frac{B_\beta}{\alpha_{ij} \alpha_{ij}}}, \quad (12)$$

where

$$\alpha_{ij} = \frac{\partial \tilde{u}_j}{\partial x_i}, \quad \beta_{ij} = \Delta_m^2 \alpha_{mi} \alpha_{mj}, \quad B_\beta = \beta_{11} \beta_{22} - \beta_{12}^2 + \beta_{11} \beta_{33} - \beta_{13}^2 + \beta_{22} \beta_{33} - \beta_{23}^2. \quad (13)$$

The model constant c_v is related to the Smagorinsky constant C_s by the relation $c_v \approx 2.5 C_s^2$. Hereafter, this model will be defined VR.

2.1.4. The subgrid fluxes

The subgrid fluxes (SGSF) were modeled according to a simple gradient diffusion (GD) approximation

$$\mathbf{b}_h = \frac{\mu_B}{Pr_t} \left(\frac{\partial \tilde{h}}{\partial x_j} \right), \quad (14)$$

where Pr_t is the turbulence Prandtl number. Here, additional case is considered in conjunction with the SGSF closure based on the classical gradient hypothesis closure and Clark's tensor diffusivity model. Within, the diffusion term in Eq. 5 was replaced in the spirit of Clark's model [9] as

$$F_d = \frac{\Delta^2}{12} \frac{\partial}{\partial x_j} \left(\frac{\partial \tilde{u}_j}{\partial x_j} \frac{\partial \tilde{k}}{\partial x_j} \right). \quad (15)$$

and the sub-grid scalar flux as

$$\mathbf{b}_h = \frac{\Delta^2}{12} \left(\frac{\partial \tilde{u}_j}{\partial x_j} \frac{\partial \tilde{h}}{\partial x_j} \right). \quad (16)$$

2.2. Numerical method

The present simulations were carried out using the OpenFoam v6.x [51] code. The governing equations were solved using the standard pressure–velocity coupling methodology and the finite-volume method based on the PIMPLE algorithm [37], which is a variation of the PISO (pressure implicit with splitting of operators) method [48]. A smooth solver (with a symmetrical Gauss-Seidel smoother) was used to compute the system of linear algebraic equations with a local accuracy of 10^{-7} for all dependent variables except pressure. The last one was calculated using the Geometric agglomerated algebraic multigrid solver (GAMG) with the Gauss-Seidel smoother and a local accuracy of 10^{-7} .

Overall, the numerical method has second-order accuracy in space and time. The convective terms were approximated by a so-called limitedLinear scheme, which belongs to the family of total variation diminishing (TVD) schemes [14], bounded with a variation of the Sweby limiter. Jasak et al. [17] have provided the details of implementation, which were described consistency recently by Robertson et al. [37] and Cao and Tamura [5]. The time integration was performed using the implicit Euler method (BDF-2 [13]). The later was accompanied by the dynamic adjustable time stepping technique to guarantee a local Courant number less than 0.4, with a typical corresponding step size, $\Delta t \approx 5 \times 10^{-7}$ s.

Aspects of high performance computing have been highlighted in authors' previous works, e.s. [21]. The Vilje high performance computing (HPC) facility (<https://www.sigma2.no/content/vilje>) was used for the present LES. Most calculations were performed using 128 – 256 cores in parallel, where typical calculation time for one time step varied between 1 – 2 s, and the total (effective) simulation time per run took around ten days.

3. Test case description

3.1. Experimental set up

The description of the Volvo test rig and relevant experimental data was provided in [42]. Fig. 1 shows a schematic drawing of the test section. The set-up consisted of a straight channel with a rectangular cross-section, divided into

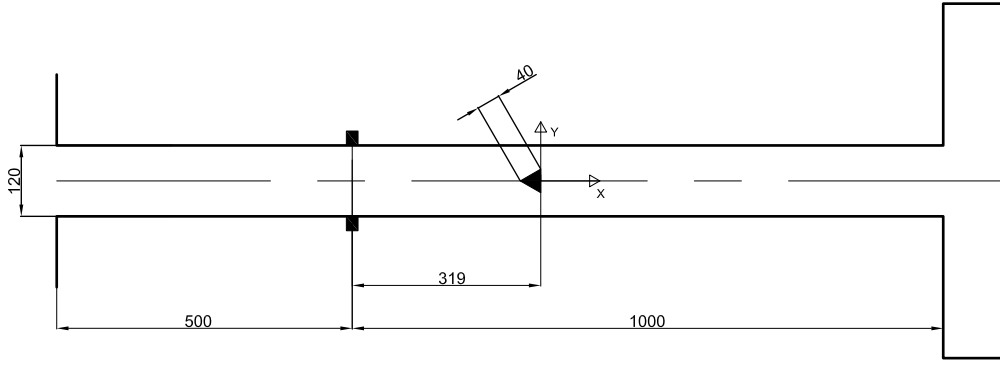


Figure 1: The sketch of the Volvo test rig. Flow direction is from left to right. All linear dimensions are in mm

an inlet section length 0.5 m and a channel passage section length $L = 1$ m and $0.12 \text{ m} \times 0.24 \text{ m}$ cross-section. The inlet section was used for flow straightening and turbulence control. The air entering the inlet section was distributed over the cross-section by a plate that, at the same time, isolated the channel acoustically from the air supply system. The channel passage section ended in a circular duct with a large diameter. The triangular cylinder (with side length, $H = 0.04$ m) was mounted with its reference position 0.681 m upstream of the channel exit. The principal flow parameters and experimental conditions are summarized in Table 1, where Re is the Reynolds number based on the triangle edge, St is the Strouhal number, U is velocity, T is temperature, p is the static pressure and L_r/H represents the recirculation zone length. The symbol ∞ denotes that a parameter is applied at the rig inlet. The Strouhal number, St , is defined as $St = f_{vs}H/U_\infty$, where f_{vs} is the vortex shedding frequency.

Table 1
Flow parameters used for the Volvo rig

Re	U_∞ [m/s]	T_∞ [K]	p_∞ [kPa]	L_r/H	St
45000	16.6	300	101	1.33	0.25

3.2. Computational domain and grids

The computational domain and the mesh strategy was inherited from the authors' previous work [21]. Here, we strongly follow [21] and provide some principal moments only. Fig. 2 shows the computational domain and the unstructured mesh (hereafter, this grid has label M1).

The computational domain consisted of three blocks. The inlet block without bluff-body was resolved by $135 \times 70 \times 45$ nodes in the stream-wise, transverse- and span-wise directions, respectively, with exponential grading of cells towards the bluff body. The central block included the obstacle and had a size of $0.2 \text{ m} \times 0.12 \text{ m}$ (Fig. 2). The bluff body edges were discretized by 75 grid points, while the stream-wise, transverse and span-wise sides of the domain were resolved by $80 \times 70 \times 45$ nodes, respectively, to obtain smooth mesh transition towards the flame holder. The remaining downstream block had a resolution of $135 \times 70 \times 45$ nodes with exponential decreasing of nodes towards the outlet.

The viscous boundary layers (BL), attached to the obstacle and the channel walls, were designed based on the first element length and the growth factor, which were set to 10^{-4} m and 1.15, both to the obstacle and wind tunnel walls. The total number of BL rows were set to 13 and 7 for the obstacle and channel walls, respectively. Finally, such combination of parameters provided the estimated minimum and averaged non-dimensional distance to the wall y^* were (0.1, 4.6) and (0.1, 5.4) for the obstacle and the channel walls, respectively.

The second grid, M2, was used to check the grid-sensitivity of the present LES results. This grid was generated by simple adaption of the baseline mesh, M1, by a factor of 1.5 in all three Cartesian directions.

The span-wise resolution for M1 and M2 grids was estimated as $dz/H = 0.134$ and $dz/H = 0.08$, respectively. On the one hand, the span-wise wavelength of stream-wise vortices in the shear layer (L_{zsl}) and in the wake (L_{zk}) could be estimated as $L_{zsl}/H \approx 0.1 \approx 25/\sqrt{Re}$ and $L_{zk}/H \approx 1$, respectively, at $Re = O(10^4)$ [52]. Based on these

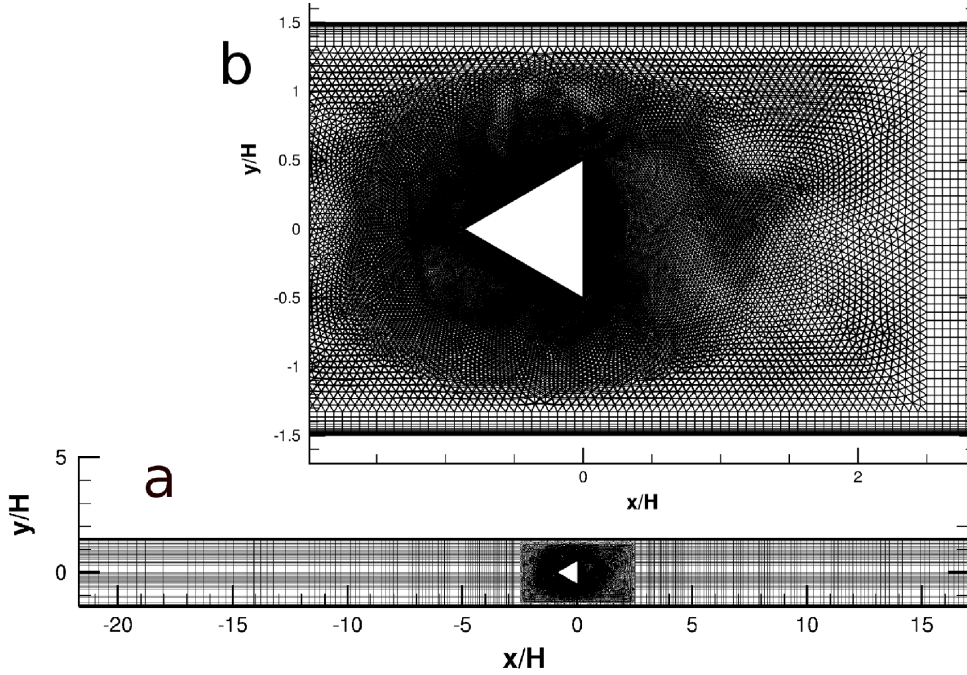


Figure 2: Description of the M1 grid in x - y (a) and its zoom at the vicinity of the bluff-body: x , y are the domain coordinates in stream-wise and transverse directions, according to the scheme on Fig. 1. z is the domain coordinate in the span-wise direction

relationships, the present mesh resolutions can be considered to be sufficient to resolve the span-wise wavelengths of the stream-wise vortices in the wake and in the shear layers for $Re = 50000$. On the other hand, Cao et al. [6] presented the more stringent criterion, $dz/H < 0.02$, to predict accurately the shear layer behaviors and the laminar-turbulent transitional process. Also, Cao et al. [6] suggested that dz/H may play some effects on development of the recirculation zone length. This tendency can be interesting and important to be analyzed in the future works, however, was not investigated in the present study due to resource limitations.

The mean drag coefficient, $\langle C_d \rangle / H$ and mean recirculation zone length $\langle L_r \rangle / H$ were chosen as the most important integral parameters to assess the grid convergence study, presented in Fig. 3. Here, the recirculation length L_r is defined as the distance between the base of the triangular cylinder ($y = 0$) and the sign change of the centerline mean stream-wise velocity. The investigation was provided for the TKE SGS model. The initial mesh was derived from M1 by reducing the grid resolution in all directions by factor 1.5 (not discussed here). One can see clearly that a deviation for both parameters as a function of a cells number was bounded by $\approx \pm 5\%$. Also, the results obtained by the Vreman SGS model, using M1 and M2 grids, were plotted in Fig. 3. It is interesting that the Vreman sub-grid scale model occurred to be more sensitive to the grid resolution. This fact can be explained by dependency of the turbulent viscosity from the squared filter width, Δ (Eq. 12-13).

3.3. Boundary conditions

The inlet and outlet boundary conditions were set up to replicate the experiment. The mean inlet velocity and temperature profiles were extracted and interpolated from URANS at the location $x/H = -2$ [21]. The inflow perturbations were not added due to the applied grid strategy, where they will be highly damped due to expansion of the grid from the bluff-body towards the inlet. A non-slipping condition for velocity was applied to the wind tunnel and the obstacle walls. The lateral boundaries were treated as the symmetry planes. The static pressure was maintained as 101 kPa. The wave-transmissive boundary condition was applied at the outlet to avoid propagating of any numerical oscillations from the outlet of the computational domain.

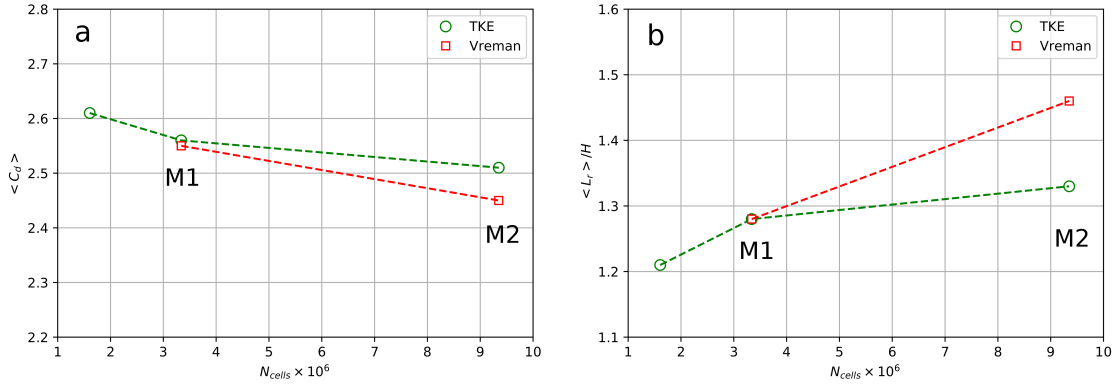


Figure 3: Dependence of the mean drag coefficient (a) and mean recirculation zone (b) on the grid size

3.4. Overview of the numerical cases

All simulated cases are listed in Table 2, where the following abbreviations are used: ID – case label, Mesh – grid label, BR – blockage ratio, SGS –subgrid scale model (dynamic k -equation eddy-viscosity sub-grid scale model (dTKE), Smagorinsky (SMAG), Vreman (VR)); SGSF – the subgrid scalar flux approximation (conventional gradient diffusion (GD) or Clark (CL)), the Reynolds number was $Re = 45000$ for all cases.

Table 2
Run matrix

ID	Mesh	BR	SGS	SGSF
VC01	M1	1/3	dTKE	GD
VC02	M2	1/3	dTKE	GD
VC03	M1	1/3	VR ($C_s = 0.1$)	GD
VC04	M2	1/3	VR ($C_s = 0.1$)	GD
VC05	M1	1/3	SMAG ($C_s = 0.053$)	GD
VC06	M1	1/3	SMAG ($C_s = 0.1$)	GD
VC07	M1	1/3	dTKE	CL
VC08	M1+	1/9	dTKE	GD
VC09	M1++	1/20	dTKE	GD

The solution is considered to be statistically converged after two and half flow-through times. The flow-through time was defined as the ratio between the axial length of the computational domain to the bulk velocity. For a quantitative validation of the present LES, the averages have been obtained from the computational results by sampling over 35 vortex shedding periods (N_{vs}) after the flow field was converged.

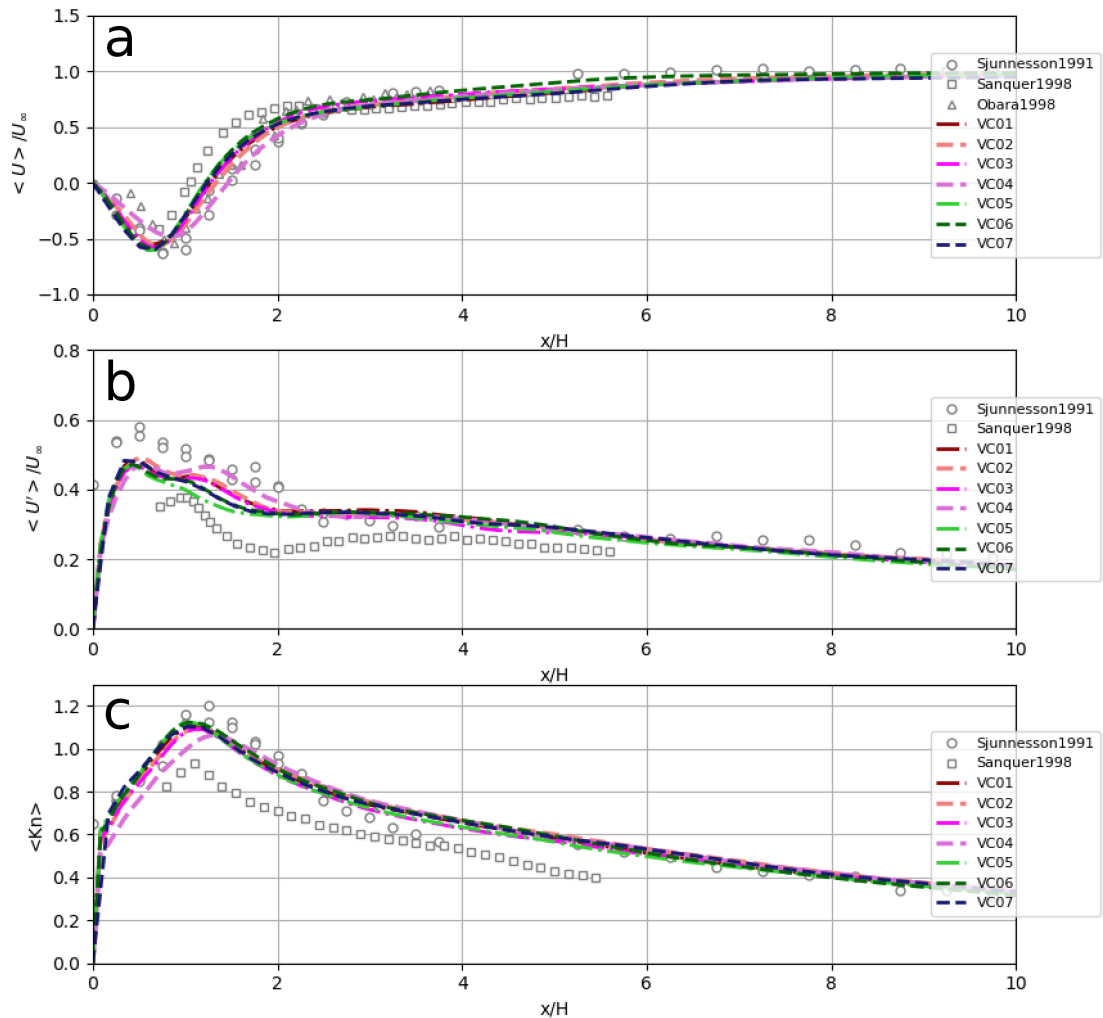


Figure 4: Mean stream-wise velocity (a), fluctuations of mean stream-wise velocity (b) and turbulence kinetic energy (c) in the wake for the flow past a triangular cylinder at $Re = 45000$

4. Results

This section presents the obtained results in terms of the first order statistics and one-dimensional spectral data. The hat, the tilde and the bar marks denoting Favre-averaging and filtering Favre-averaging were omitted for simplicity.

4.1. First order statistics

Figure 4 shows the measured and calculated mean stream-wise velocity, fluctuations of the mean stream-wise velocity and the normalized subgrid turbulence kinetic energy along the center-line behind the obstacle. For the sake of completeness, besides the experimental results by Sjunnesson et al. [42], the LDV data by Sanquer et al. [39] and Obara et al. [31] were added.

Overall, there was a good agreement between numerical and experimental data. One can observe the same trends between all numerical runs for the axial distribution of the mean stream-wise velocity, except the VC04 case, which provided some discrepancies. The normalized turbulence kinetic energy, $K_n = \sqrt{k}/U_\infty$, where the turbulence kinetic energy $k = 3/4 (U'^2 + V'^2)$, following the experiments of Sjunnesson et al. [42], is shown in Fig. 4,c. It was a fairly good agreement between all numerical runs and experimental data.

Comparison of first order statistics against experimental data by Sjunnesson et al. [42] for the near wake at three

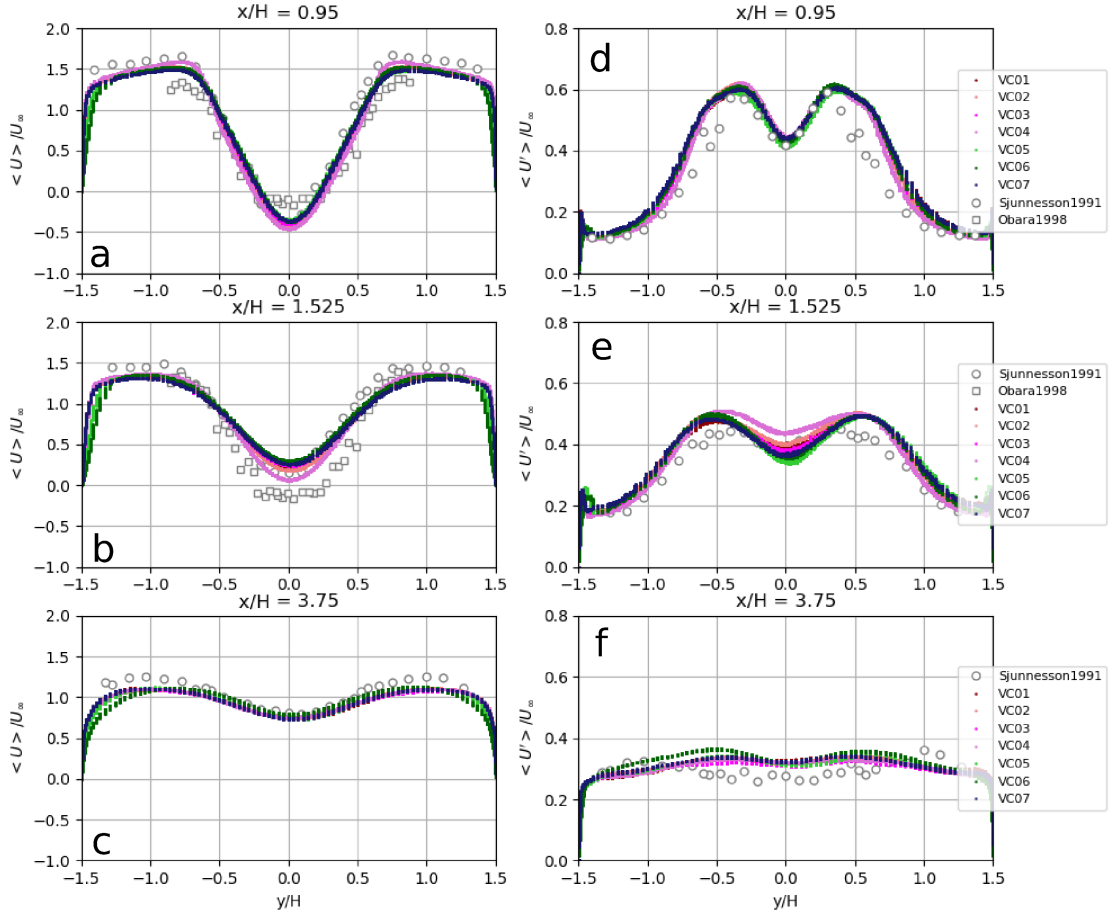


Figure 5: Mean stream-wise velocity (a,b,c) and its root-mean-square (d,e,f) at several locations ($x/H = 0.95, 1.525, 3.75$) in the wake of the flow over triangular cylinder at $Re = 45000$

different downstream locations ($x/H = 0.95, 1.525, 3.75$) is provided in Figure 5. Fig. 5,a-c shows profiles for the mean stream-wise velocity $\langle U \rangle / U_\infty$. One can see that the present calculations agreed with the LDV measurements of Sjunnesson et al. [42] quite satisfactory for all three axial states. The experimental data by Obara et al. [31] was added as well for $x/H = 0.95$ and $x/H = 1.525$. It worth noting, that the LDV data by Obara et al. [31] was obtained for $Re = 75000$ based on the non-equilateral triangular cylinder. Moreover, the blockage ratio was different between these two experiments, which may explain several discrepancies observed in Fig. 5,a,b.

In Figure 5,d-f the RMS values of the stream-wise velocity $\langle U' \rangle / U_\infty$ are shown. The transitional nature of the shear layers resulted in the primary vortex formation [34] and can be observed in the $\langle U' \rangle$ profile with two strong peaks at $x/H = 0.95$. The same type of the $\langle U' \rangle$ profile can be observed at $x/H = 1.525$. Finally, at $x/H = 3.75$, the $\langle U' \rangle$ profile was more or less flat outside of the mean recirculation zone. It was observed that all SGS models collapsed well to reproduce the experiment by Sjunnesson et al. [42]. Some small deviations were observed between the present LES and the LDV data but, in general, satisfactory agreement between numerical and experimental results was achieved.

Significant deviations between the recirculation zone length L_r , obtained in numerical simulations and measurements are often observed for many turbulent bluff-body flows. Typical flow patterns are displayed in Fig. 6. The present results converged to $L_r/H = 1.28 \pm 9\%$, which was reasonably close to the experimental data by Sjunnesson et al.[42], who measured $\langle L_r \rangle / H = 1.35$. The minimum L_r was obtained by the SMAG model $L_r/H = 1.21$. The calculated values by dTKE and VR models were in the range $L_r/H = 1.24 - 1.46$. However, the available experimental works provided a large scattering of data, $L_r/H = 1.35 - 1.8$. The large variation in measurements can be

explained by transitional effects in the separating shear layers, reproduced by different setup of the wind tunnels and flow conditions.

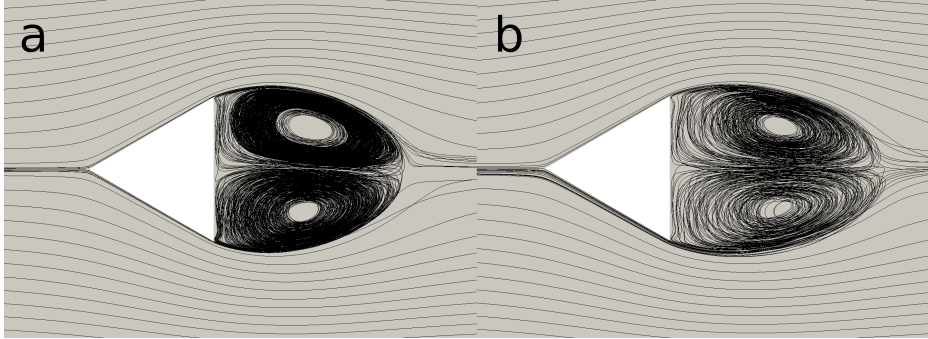


Figure 6: Time-averaged (not averaged in a span-wise direction) streamlines in the midsection of the computational domain for the flow over a triangular cylinder at $Re = 45000$: VC02 (a) and VC04 (b)

4.2. One-dimensional energy spectra

Based on the moderate Reynolds number, $Re = 45000$, this flow can be attributed to the ‘sub-critical regime’, where the separated boundary layer stays laminar for $Re < 200000$. Figure 7 illustrates the formation of the vortex street and coherent flow structures downstream of the bluff-body, showing the Q -criterion, $Q = S^2 - \Omega^2 = 10^6$, where S is the strain rate and Ω is the vorticity. The visualization displays the capability of the present LES to resolve wide range of energetic flow structures, developed in the turbulent wake.

The vortex shedding instability can be expressed by a characteristic frequency, $f_{vs} = StU_\infty/H$, based on the Strouhal number, St . To compute both characteristic frequencies of the vortex shedding and Kelvin-Helmholtz (KH) instability, the velocity signals were sampled in probes located at the vicinity of the bluff-body at $x/H = 1.75$ and $y/H = 0$. In addition, probes were located in places, where the shear layer instabilities develops from both sides of the cylinder. About $1.5 \cdot 10^5$ samples of the cross-flow velocities were collected over a dimensionless time interval $t^* = tU_\infty/H \approx 100$ (or $N_{vp} = t/f_{fs} \approx 35$). The spectra calculated from these time series were then averaged in the span-wise direction (nine probe locations uniformly distributed were used) to increase the statistical meaning. To obtain the one-dimensional spectra, both Fast Fourier transform (FFT) and the Welch periodogram technique [50] were used.

The computed value of the Strouhal number of the vortex shedding frequency was $St = 0.27 \pm 1.3\%$, which was found to be slightly over-estimated (by 7.4%) compared to the experimental data by Sjunnesson et al. [42], who predicted $St = 0.25$. Alternative experimental data, provided in Table 3, showed a variation of the Strouhal between $0.21 - 0.26$. Over-estimation of the vortex shedding frequency by the present LES may be explained by the numerical effects, related to the vortices quenching and their interaction with the channel walls.

Figure 8,a compares one-dimensional, nondimensionalized frequency spectra at the downstream location ($x/H = 1.75$) on the centerline of the wake. The experimental results of Ong and Wallace [33], Sanquer et al. [39] and Parnaudeau et al. [34] were plotted as well as a $-5/3$ slope. All present numerical results yielded very similar power spectra, where the inertial subrange was reproduced for a quite large spectral range. One critical remark should be made here. Based on the spectra displayed in Fig. 8,a, it can be observed that the TVD scheme produced some ‘unnatural’ energy spectra, as was originally discussed by Cao and Tamura [5]. They observed that the TVD scheme seems to exhibit different influences on the spectral curves, tending to reduce the energy in the inertial subrange and increase energy in the dissipation range.

The separated shear layer behaves in a similar manner to a mixing layer, when the recirculation zone length is sufficiently long. The shear-layer instability is based on the Kelvin-Helmholtz mechanism (and the characteristic frequency, f_{kh}) for $Re > 1200$, leading to shear layer roll-up into tightly concentrated vorticity [41]. From the experimental point of view, several studies investigating the separated shear-layer from the circular cylinder are available in the literature [1], [25], [18], [30], [27], [35], [36]. Bloor [1] seems to be the first who studied the frequency of the shear layer instability waves. She demonstrated that the shear layer instability frequency scaled approximately with \sqrt{Re} , by considering the thickness and velocity of the separating laminar boundary layer. Lately, Prasad and Williamson [35] provided

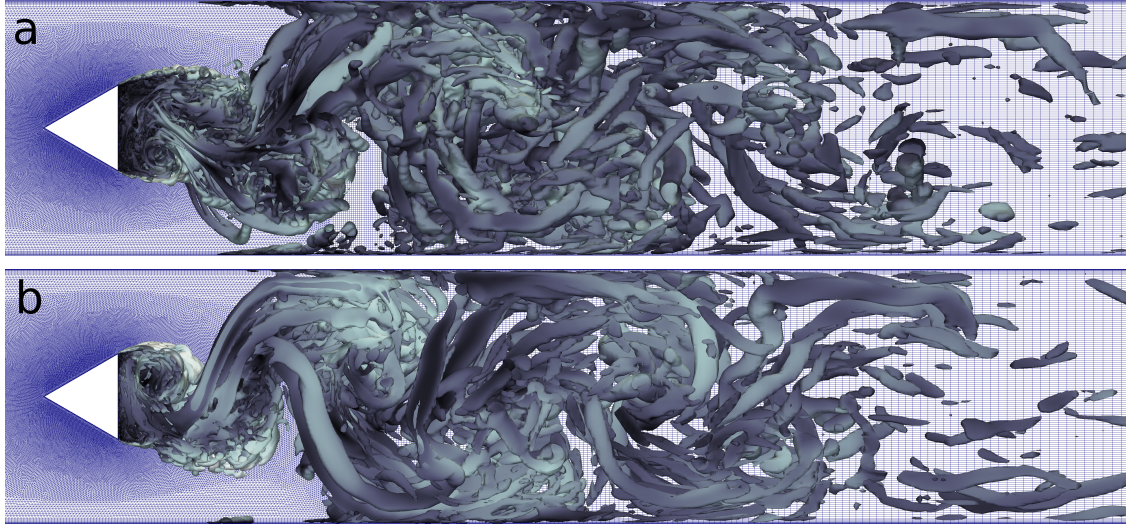


Figure 7: Visualization of flow structures obtained for the flow past a triangular cylinder at $Re = 45000$: VC02 (a) and VC04 (b) runs, respectively. Iso-surfaces of the Q -criterion ($Q = S^2 - \Omega^2 = 10^6$, where S is the strain rate and Ω is the vorticity)

Table 3

Overview of prime parameters and integral flow features of the triangular cylinder flow: experimental and numerical (LES) results

Contributor	Method	BR	$\langle C_d \rangle$	$\langle -C_l \rangle$	$\langle -C_{pb} \rangle$	$\langle L_r \rangle / H$	St	Re
Okamoto et al. [32]	HWA	1/40	1.26		1.09	1.8	0.21	22000
Tatsuno et al. [44]	HWA	1/29	1.4		1.38			90000
Sjunnesson et al. [42]	LDV	1/3				1.35	0.25	45000
Sanquer et al. [39]	LDV	1/3				≈ 1	0.26	5828
Obara et al. [31]	LDV						0.26	75000
Yagmur et al. [53]	PIV	1/12					0.225	11600
Yagmur et al. [53]	LES	1/9.5	1.436			1.6	0.219	11600
Zheng et al. [57]	PIV	1/4				1.7	0.21	14400
Fujii et al. [11]	LDV	1/2			2.73	2.2	0.4	17500
Calvert [3]	HWA	1/10			0.375	1.85	0.171	50000
VC01	LES	1/3	2.56	-0.0001	2.23	1.28	0.27	45000
VC02	LES	1/3	2.51	-0.0002	2.19	1.33	0.27	45000
VC03	LES	1/3	2.55	-0.0011	2.18	1.28	0.25	45000
VC04	LES	1/3	2.45	-0.0008	2.12	1.46	0.27	45000
VC05	LES	1/3	2.65	-0.0025	2.21	1.21	0.28	45000
VC06	LES	1/3	2.69	-0.0021	2.17	1.21	0.29	45000
VC07	LES	1/3	2.61	-0.0040	2.26	1.24	0.26	45000
VC08	LES	1/9	1.51	-0.0011	1.25	1.42	0.20	45000
VC09	LES	1/20	1.42	-0.0031	1.09	1.42	0.21	45000

re-evaluation of all data and reported that the exponent p in the expression $f_{kh}/f_{vs} = A \times Re^p = 0.0235 \times Re^{0.67}$ was significantly greater than 0.5 in every case. Dynamics of the shear layer transition of a square cylinder at the Reynolds number range $15000 < Re < 75000$ have been investigated by Lander et al. [19]. They derived the relation $f_{kh}/f_{vs} = 0.18 \times Re^{0.6}$, which was based on the hot-wire measurements, PIV and DNS studies. The numerical data of Brun et al. [2] and Trias et al. [46] were analyzed as well. These data were obtained at $Re = 20000$ (LES), $Re = 22000$ (Direct numerical simulation) and $Re = 27000$ (laser Doppler velocimetry, LDV).

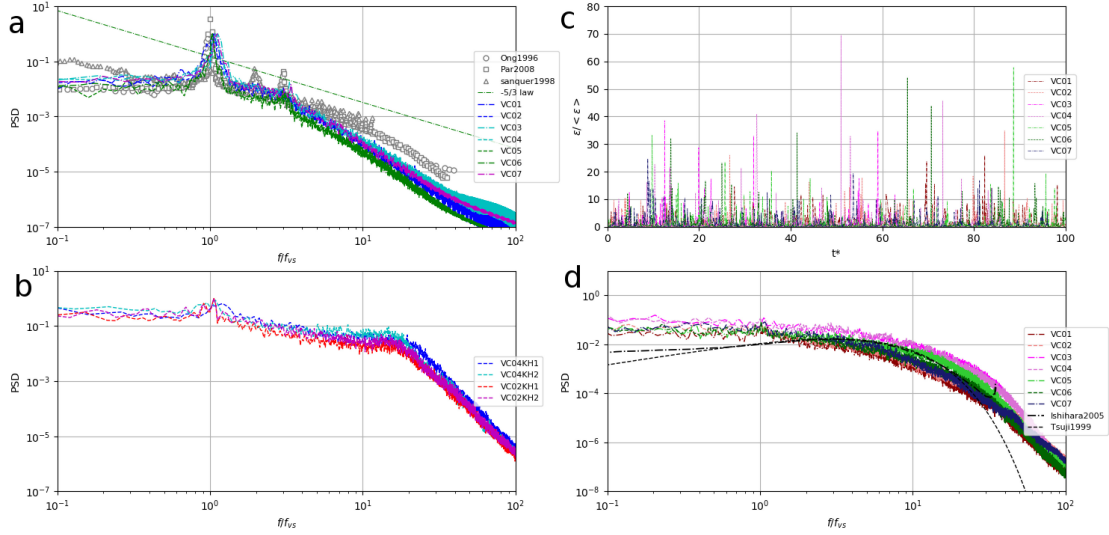


Figure 8: One-dimensional spectra of the transverse velocity in the near wake at the points $x/H = 1.75, y/H = 0$ (a) and $x/H = 0.35, y/H = \pm 0.55$ (b). Time history of the turbulence kinetic energy dissipation rate, ϵ (c) and its one-dimensional energy spectra (d), obtained at the point $x/H = 1.75, y/H = 0$

Recently, Moore et al. [29] carried out a detailed experimental study of the separated shear layers stemming from rectangular sections with aspect ratios of $5 : 1, 3 : 1$ and $1 : 1$ in the range $13400 < Re < 118000$ (the Reynolds number was based on the body thickness). It was interesting that experimental results for f_{kh}/f_{vs} obtained by Moore et al. [29] for the $5 : 1$ rectangular section was somewhere between the square prism and circular cylinder. Some limited compiled data are plotted in Figure 9. Moore et al. [29] reported that all geometries fit well with a power law. However, both the exponent and the coefficient are different for each bluff-body geometry.

The authors' previous LES results calculated for the circular cylinder flow revealed $f_{kh}/f_{vs} = 7.6$ and $f_{kh}/f_{vs} = 16.2$ for $Re = 3900$ [22] and $Re = 20000$ [24], respectively. These results were in good agreement with the available experimental data and numerical data [10]. In addition, the DNS study by Trias et al. [46] provided for the square prism at $Re = 22000$ a relatively broadband frequency peak at $f_{kh}/f_{vs} \sim 60$. Cao and Tamura [4] calculated the peaks of shear-layer frequencies as $f_{kh}/f_{vs} = 15 - 17$, which were much smaller than the LDV measurement by Minguez et al. [28] ($f_{kh}/f_{vs} \sim 45$).

The present LES results obtained for the equilateral triangular cylinder predicted $f_{kh}/f_{vs} = 13.74 - 16.01$. Figure 8,b presents the Welch spectra computed for VC02 and VC04. These results were close to the experimental trend obtained for the circular cylinder.

4.3. Note on turbulence kinetic energy dissipation rate

The time history of the turbulence kinetic energy dissipation rate, normalized by the mean, $\epsilon/\langle\epsilon\rangle$ is displayed in Figure 8,c. It is interesting that the numerical signals qualitatively reproduced the experimental signals of ϵ obtained respectively in a laboratory boundary layer and in the atmospheric surface layer by Meneveau and Sreenivasan [26]. In the present study, the term F_ϵ (Eq. 8) has been sampled for each run at the location, $x/H = 1.75, y/H = 0$. In the same spirit as for the velocity signals, FFT and the Welch periodogram technique were applied to plot the one-dimensional energy spectra, provided in Fig. 8,d. Results of the high resolution DNS by Ishihara et al. [16] and the dissipation spectra measured by Tsuji [47] are added to compare the present LES.

The model for the turbulence kinetic energy dissipation rate (Eq. 8) relies on the assumption that for a fixed Δ , ϵ scales as $k^{3/2}$. In general, the power law scaling $\epsilon \sim k^\gamma$ has been observed in several experimental studies assuming that γ is constant. Based on DNS of forced isotropic turbulence Chumakov [8] found, that the scaling assumption $\epsilon \sim k^\gamma$ holds reasonably well for SGS Reynolds numbers of up to 5000. However, the value of γ was not found to be a constant, but to dependent on the proximity of the filter size, Δ to the forcing length scale. Chumakov [8] reported that none of the observed scalings were close to $\epsilon \sim k^{3/2}$, which is widely used in the literature. He found that $\gamma \approx 1/2$ for

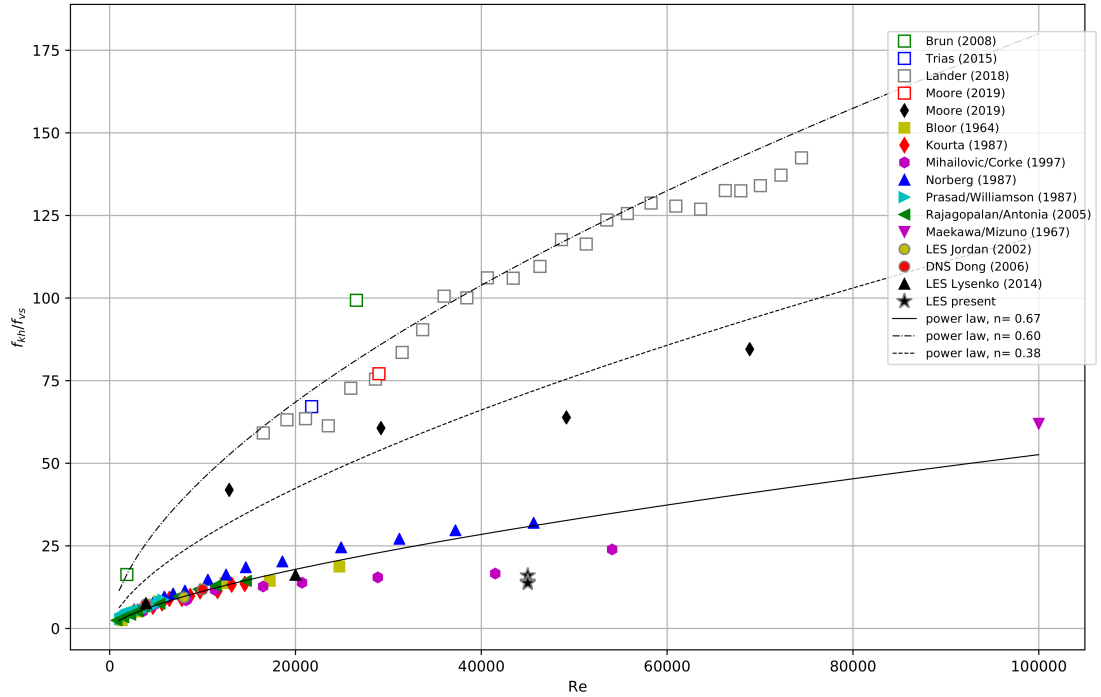


Figure 9: Variation of normalized shear layer frequency with Reynolds number: experimental and computational results

Δ close to forcing scale and $\gamma \approx 1$ for Δ in the near-viscous range, in accordance with Meneveau and O’Neal [26]. In the inertial subrange, γ varied between 0.6 – 0.9 monotonically with Δ . It is worth noting that the present LES results revealed the spread of γ between 0.76 – 0.89 in spite of the fact that Eq. 8 was used to sample the dissipation rate. This fact is demonstrated in Figure 10. Moreover, the coefficient c_ϵ from Eq. 8, was computed dynamically for each LES run. Figure 11 displays variation of the mean c_ϵ depending on the SGS model. It is interesting to see that c_ϵ can deviate significantly from its widely used value, $c_\epsilon = 1.048$. The present results showed that c_ϵ maximum may reaches $c_\epsilon = 30$ in some regions of the computation domain.

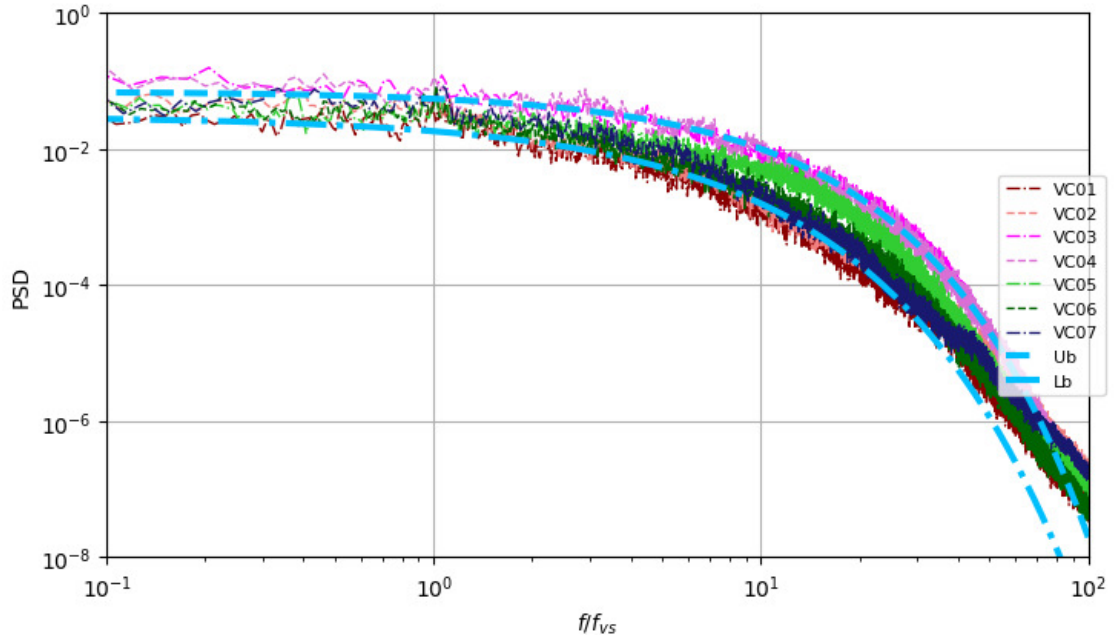


Figure 10: Variation of the one-dimensional spectra of the turbulence kinetic energy dissipation rate, ϵ for the flow over a triangular cylinder at $Re = 45000$. U_b and L_b correspond to $\epsilon \sim k^{0.89}$ and $\epsilon \sim k^{0.77}$, respectively

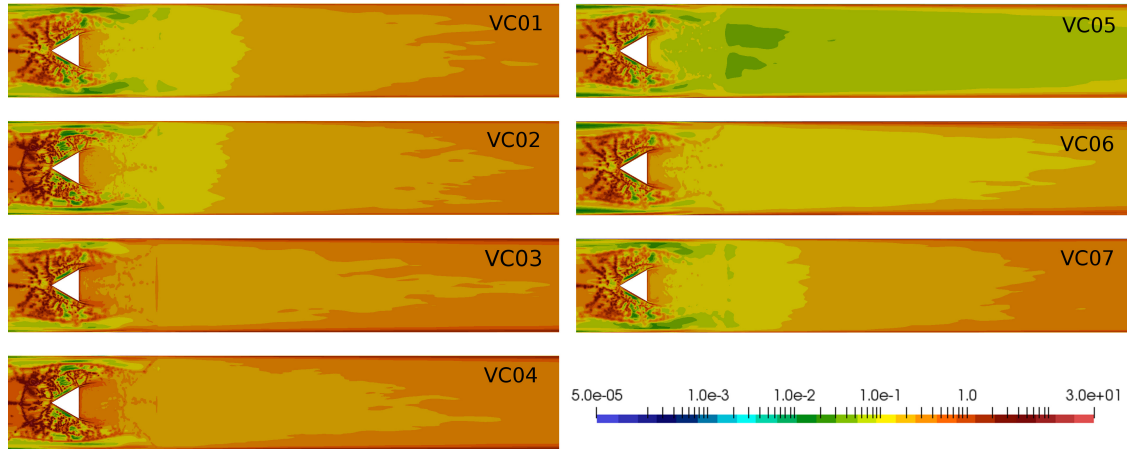


Figure 11: Contours of the time-averaged coefficient, c_e , computed in the middle cross-section of the computational domain for the flow over a triangular cylinder at $Re = 45000$

5. Discussion

6. Overview

High fidelity LES on relatively coarse grids is important for practical engineering applications. Several modeling aspects may be considered. On one hand, when coarse grids are used in LES, the effect of the numerical modeling on the flow resolution is increased [20]. On the other hand, effects of the subgrid modeling become more pronounced as well. The unstructured grid strategy, which is attractive for any practical applications due to ability to focus the refinement more effectively, is better designed for isotropic eddy-viscosity turbulence models [20]. However, the sudden change in cell size across refinement region boundaries may be an issue, and special considerations for the grid

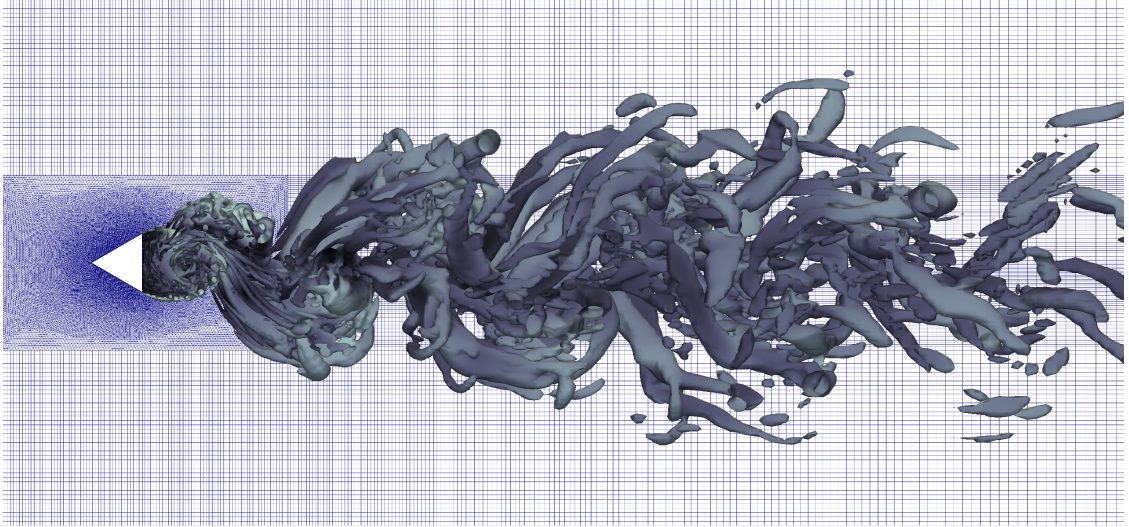


Figure 12: Iso-surfaces of the Q -criterion ($Q = 10^5$) calculated for VC08 for the flow over a triangular cylinder at $Re = 45000$

design should be taken into account, e.g, by placed these interfaces away from key flow features.

Table 3 incorporates integral flow parameters collected from available experimental and numerical (LES) results. In general, flow physics, which characterize the turbulent separated flow past a bluff-body at the moderate Reynolds number, was captured well in the present numerical simulation. The present numerical results obtained by the different algebraic SGS models were quite consistent with the dispersion of about 10% for the main integral quantities. Reasonable deviations were found for the first order statistics. Overall, the present study matched reasonably well the corresponding experimental data [42].

However, some important flow parameters like the drag and pressure coefficients were missed in the experimental data by Sjunnesson et al.[42]. Also, this particular experiment was performed in the wind tunnel channel with blockage ratio, $BR = 1/3$. It is well known, that blockage and interference effects need to be considered. These effects may be relatively low but certainly affect the measured drag and pressure coefficients (and other related parameters) [46].

6.1. Blockage effects

Most blockage theories make the assumption that the principal effect is an increase in free-stream velocity and consequently fall in static pressure [3]. For the sake of completeness, we performed the additional LES run (VC08) to investigate the blockage effects. For this case, the baseline grid, M1, was extended by top and bottom buffer domains to decrease the blockage to $BR = 1/9$ and $BR = 1/20$, keeping the free-stream Re and M numbers the same. Furthermore, the alternative HWA measurements by Calvert [3] were used to assess sensitivity results to the BR effects.

Figure 12 provides the instantaneous flow visualization based on the Q -criterion and some aspects of the grid for $BR = 1/9$. One can clearly see the difference in the flow fields obtained for $BR = 1/3$ and $BR = 1/9$, displayed in Figures 7 and 12, respectively. The calculated Strouhal numbers $St = 0.20 - 0.21$ were indicating that the vortex shedding formation was significantly less intensive for the unconfined cases. Also, this value agreed reasonably with the data reported by Okamoto et al. [32] ($St = 0.21$), Zheng et al. [57] ($St = 0.21$) and Yagmur et al. [53] ($St = 0.219 - 0.225$). It is worth noting that the experimental studies demonstrated the clear tendency on decreasing of St with decreasing of BR . Thus, Fujii et al. [11] provided $St = 0.4$ for $BR = 1/2$. Sjunnesson et al.[42] and Sanquer et al.[39] measured $St = 0.25 - 0.26$ for $BR = 1/3$. Other researchers presented $St = 0.171 - 0.225$ for $BR < 1/3$ ([3], [32], [57], [53]).

The time-averaged pressure coefficient ($C_p = \frac{2(p-p_\infty)}{\rho_\infty U_\infty^2}$, where p_∞ and ρ_∞ are the free stream pressure and density, respectively) at the surface of a triangular cylinder is displayed in Fig. 13,a. The results of VC01 ($BR = 1/3$), VC08 ($BR = 1/9$) and VC09 ($BR = 1/20$) are compared against the experimental data by Tatsuno et al. [44] and Okamoto et al. [32].

The calculated integral values of the base suction coefficient for $BR = 1/9$ and $BR = 1/20$ were $\langle -C_{pb} \rangle = 1.25$

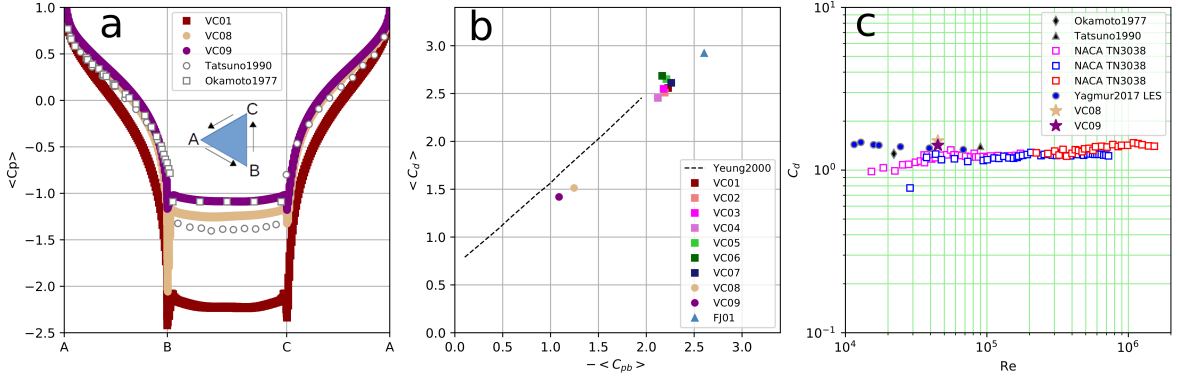


Figure 13: Time-averaged pressure coefficient distribution on a cylinder surface (a), the $C_{p,b}-C_d$ dependence (b) and the integral $Re-C_d$ results(c)

and 1.09, which correlated reasonably with the experimental value obtained by Tatsuno et al. [44] and Okamoto et al. [32], who measured $-C_{p,b} = 1.38$ and $-C_{p,b} = 1.09$, respectively. Also, Calvert [3] presented a significantly different value, $-C_{p,b} = 0.375$. The calculated base suction coefficient for $BR = 1/3$ was $\langle -C_{pb} \rangle = 2.19 \pm 4.5\%$.

The base suction coefficient is strongly related to the drag coefficient ($C_d = \frac{2F_D}{\rho_\infty U_\infty^2 A}$, where F_D is the drag force in the stream-wise direction and A is the projection area of the front view). The calculated drag coefficients for $BR = 1/9$ and $BR = 1/20$ were $\langle C_d \rangle = 1.51$ and 1.42 , which matched reasonably the experimental and numerical results available in the literature. Okamoto et al. [32] presented $C_d = 1.26$ for the Reynolds number, $Re = 22000$. Tatsuno et al.[44] reported $C_d = 1.4$ for $Re = 90000$. Recently, Yagmur et al. [53] reported $C_d = 1.43$ using LES for $Re = 11600$. All these values were quite close to the data provided by NACA TN3038. Figure 13,c summarizes these findings. The calculated drag coefficients for $BR = 1/3$ were significantly higher, $\langle C_d \rangle = 2.57$ with a dispersion of 8%.

Yeung and Parkinson [54] developed and reported an analytical dependence of the drag versus the base suction coefficient. This dependence has a linear distribution for the triangular cylinders and wedges and is displayed in Figure 13,b. The present LES results are plotted in the same figure and were tending to the similar distribution. The experimental data by Fujii et al. [11], who reported $-C_{p,b} = 2.67$ for $BR = 1/2$, satisfied this tendency as well.

The first-order statistics obtained for $BR = 1/20, 1/9, 1/3$ are displayed in Figure 14, together with the available experimental data by Calvert [3] and Sjunnesson et al.[42]. For the sake of completeness, we added the PIV measurements by Yagmur et al. [53] and LDV data by Sanquer et al.[39] and Obara et al. [31]. In general, the discrepancies observed between numerical results by VC08, VC09 and VC01 were tending only to a small permanent bias, which may be explained by the similarity of the numerical method used for both LES calculations. However, more pronounced differences can be found between the HWA data by Calvert [3] and the LDV measurements by Sjunnesson et al.[42], meaning that setup of the physical experiment and properties of the wind tunnel test section affected the results. It worth notice that numerical results obtained for VC08 and VC09 matched reasonably, indicating only small influence of the blockage effects on the downstream wake for $BR < 1/9$.

7. Conclusions

A large eddy simulation of the turbulent flow over an equilateral triangular cylinder at Reynolds number, $Re = 45000$ (based on the triangle edge) has been performed to replicate the well-known experimental of the Volvo test rig. A fully-conservative finite-volume method of the second-order accuracy in space and time, based on the OpenFoam technology, was used. The family of the algebraic, eddy-viscosity SGS models, including the conventional Smagorinsky, Vreman and dynamic version of k -equation, has been assessed in the present study.

Time-averaged results have been presented and compared against experimental data. The agreement with the LDV measurements in the wake region for the mean stream-wise velocity and its fluctuation was rather good. The axial distribution of the turbulence kinetic energy matches experimental data reasonably well, suggesting that the present LES resolved a significant part of the turbulent scales. Integral flow characteristics like the mean drag and surface pressure coefficients have been compared against alternative measurements available in the literature. The agreement

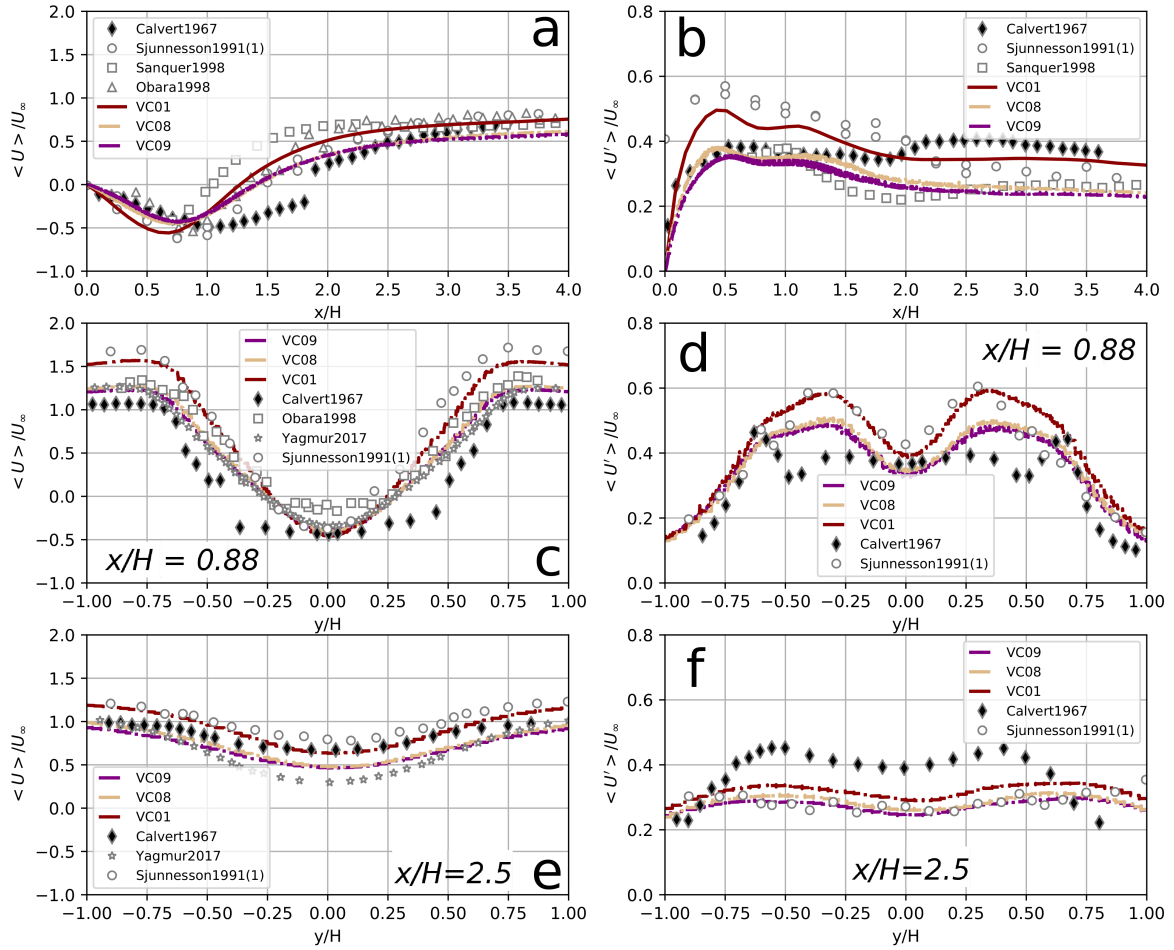


Figure 14: The Blockage effects on the axial (a,b) and traversal (c-f) distribution of the mean stream-wise velocity and its fluctuation for the flow over a triangular cylinder at $Re = 45000$

was quite satisfactory, in spite the slightly different flow setup and conditions.

Finally, the spectral analysis of the velocity samples has been carried out to compute both the KH and Von Kármán instabilities. The numerical predicted Strouhal numbers were in a fairly good agreement with the measured, indicating that the weak dynamics were well captured. However, comparison of the energy spectra showed that the numerical method was slightly over-dissipative, which may be explained by application of the TVD scheme and unstructured grids, artificially tending to reduce the energy at the low frequencies and increase energy at the higher frequencies. These finding supports the observations of Cao and Tamura [5]. Furthermore, it was found that the turbulence kinetic energy dissipation rate scaled according to the power law with $\gamma = 0.77 - 0.89$ unlikely to the widely used value, $\gamma = 3/2$.

Overall, the above-mentioned good agreement of the integral flow features and turbulence statistics that the bluff-body flow physics is well reproduced. All SGS models are agreed reasonably well between each others, with some minor differences with dispersion of $\approx 10\%$.

References

- [1] Bloor, M., 1964. The transition to turbulence in the wake of a circular cylinder. *J. Fluid Mech.* 19, 290–304.
- [2] Brun, C., Aubrun, S., Goossens, T., Ravier, P.H., 2008. Coherent structures and their frequency signature in the separated shear layer on the sides of a square cylinder. *Flow Turbul. Combust* 81, 97–114.
- [3] Calvert, J.R., 1967. Experiments on the low-speed flow past cones. *J. Fluid Mech.* 27(2), 373–289.

- [4] Cao, Y., Tamura, T., 2015. Numerical investigations into effects of three-dimensional wake patterns on unsteady aerodynamics characteristics of a circular cylinder at $Re = 1.3 \times 10^5$. *J. Fluids Struct.* 59, 351–369.
- [5] Cao, Y., Tamura, T., 2016. Large-eddy simulations of flow past a square cylinder using structured and unstructured grids. *Comput. Fluids* 137, 36–54.
- [6] Cao, Y., Tamura, T., Kawai, H., 2020. Spanwise resolution requirements for the simulation of high-Reynolds-number flows past a square cylinder. *Comput. Fluids* 196, 104–320.
- [7] Chaouat, B., 2017. The state of the art of hybrid RANS/LES modeling for the simulation of turbulent flows. *Flow Turbul. Combust.* 99, 279–327.
- [8] Chumakov, S.G., 2007. Scaling properties of subgrid-scale energy dissipation. *Phys. Fluids* 19, 058104.
- [9] Clark, R.A., Ferziger, J.H., Reynolds, W.C., 1979. Evaluation of subgrid-scale models using an accurately simulated turbulent flow. *J. Fluid Mech.* 91, 1–16.
- [10] Dong, S., Karniadakis, G.E., Ekmekci, A., Rockwell, D., 2006. A combined direct numerical simulation particle image velocimetry study of the turbulent air wake. *J. Fluid Mech.* 569, 185–207.
- [11] Fujii, S., Gomi, M., Eguchi, K., 1978. Cold flow tests of a bluff-body flame stabilizer. *J. Fluid Engineering.* 100, 323–332.
- [12] Fureby, C., 1996. On subgrid scale modeling in large eddy simulations of compressible fluid flow. *Phys. Fluids* 8(5), 1301–1311.
- [13] Geurts, B., 2004. *Elements of Direct and Large-Eddy Simulation*. R.T.Edwards, Philadelphia.
- [14] Harten, A., 1983. High resolution schemes for hyperbolic conservation laws. *J. Comput. Phys.* 49, 357–393.
- [15] Horiuti, K., 1985. Large eddy simulation of turbulent channel flow by one-equation modeling. *J. Phys. Soc. Japan* 54(8), 2855–2865.
- [16] Ishihara, T., Kaneda, Y., Yokokawa, M., Itakura, K., Uno, A., 2005. Energy spectrum in the near dissipation range of high resolution direct numerical simulation of turbulence. *J. Phys. Society Japan* 74(5), 1464–1471.
- [17] Jasak, H., Weller, H.G., Gosman, A.D., 1999. High resolution nvd differencing scheme for arbitrarily unstructured meshes. *Int. J. Numer. Methods* 31, 431–449.
- [18] Kourta, A., Boisson, H., Chassing, P., 1987. Non-linear interactions and the transition to turbulence in the wake of a circular cylinder. *J. Fluid Mech.* 181, 41–161.
- [19] Lander, D.C., Moore, D.M., Letchford, C.W., Amitay, M., 2018. Scaling of square-prism shear layers. *J. Fluid Mech.* 849, 1096–1119.
- [20] Lloyd, T.P., James, M., 2016. Large eddy simulations of a circular cylinder at Reynolds numbers surrounding the drag crisis. *Applied Ocean Research* 59, 676–686.
- [21] Lysenko, D.A., Ertesvåg, I.S., 2018. Reynolds-averaged, Scale-Adaptive and Large-eddy simulations of premixed bluff-body combustion using the Eddy Dissipation Concept. *Flow Turbul. Combust.* 100, 721–768.
- [22] Lysenko, D.A., Ertesvåg, I.S., Rian, K.E., 2012. Large-eddy simulation of the flow over a circular cylinder at Reynolds number 3900 using the OpenFOAM toolbox. *Flow Turbul. Combust.* 89, 491–518.
- [23] Lysenko, D.A., Ertesvåg, I.S., Rian, K.E., 2013. Modeling of turbulent separated flows using OpenFOAM. *Comput. Fluids* 80, 408–422.
- [24] Lysenko, D.A., Ertesvåg, I.S., Rian, K.E., 2014. Large-eddy simulation of the flow over a circular cylinder at Reynolds number 2×10^4 . *Flow Turbul. Combust.* 92, 673–698.
- [25] Maekawa, T., Mizuno, S., 1967. Flow around the separation point and in the near wake of a circular cylinder. *Phys. Fluids (Supp.)*, 184–186.
- [26] Meneveau, C., R., S.K., 1991. The multifractal nature of turbulent energy dissipation. *J. Fluid Mech.* 224, 429–484.
- [27] Mihailovic, J., Corke, T.C., 1987. Three-dimensional instability of the shear layer over a circular cylinder. *Phys. Fluids* 9(11), 3250–3257.
- [28] Minguez, M., Brun, C., Pasquetti, R., Serre, E., 2011. Experimental and high-order LES analysis of the flow in near-wall region of a square cylinder. *Int. J. Heat Fluid Flow* 32, 558–566.
- [29] Moore, D.M., Letchford, C.W., Amitay, M., 2019. Energetic scales in a bluff body shear layer. *J. Fluid Mech.* 875, 543–575.
- [30] Norberg, C., 1987. Effects of Reynolds number and a low intensity free stream turbulence on the flow around a circular cylinder, in: *Publication No. 87/2*, Chalmers University of Technology, Sweden.
- [31] Obara, H., Matsudaira, Y., 1998. Large vortex formation-mechanism behind wedge under several separation conditions. *JSME Series B* 41(4), 788–795.
- [32] Okamoto, T., Yagita, M., Ohtsuka, K., 1977. Experimental investigation of the wake of a wedge. *JSME* 20(141), 323–328.
- [33] Ong, L., Wallace, J., 1996. The velocity field of the turbulent very near wake of a circular cylinder. *Exp. Fluids* 20, 441–453.
- [34] Parnaudeau, P., Carlier, J., Heitz, D., Lamballais, E., 2008. Experimental and numerical studies of the flow over a circular cylinder at Reynolds number 3900. *Phys. Fluids* 20(8).
- [35] Prasad, A., Williamson, C.H.K., 1997. The instability of the shear layer separating from a bluff body. *J. Fluid Mech.* 333, 375–402.
- [36] Rajagopalan, S., Antonia, R.A., 2005. Flow around a circular cylinder-structure of the near wake shear layer. *Exp. Fluids* 38, 393–402.
- [37] Robertson, E., Choudhury, V., Bhushana, S., Walters, D.K., 2015. Validation of OpenFOAM numerical methods and turbulence models for incompressible bluff body flows. *Comput. Fluids* 123, 122–145.
- [38] Sagaut, P., 2006. *Large Eddy Simulation for incompressible flows*. 3rd ed., Springer Berlin.
- [39] Sanquer, S., Bruel, P., Deshaies, B., 1998. Some specific characteristics of turbulence in the reactive wakes of bluff bodies. *AIAA J.* 36(6).
- [40] Schumann, U., 1975. Subgrid scale model for finite difference simulations of turbulent flows in plane channels and annuli. *J. Comput. Phys.* 18, 376–404.
- [41] Shanbhogue, S.J., Husain, S., Lieuwen, T., 2009. Lean blowoff of bluff body stabilized flames: scaling and dynamics. *Prog. Energy Combust. Sci.* 35, 98–120.
- [42] Sjunnesson, A., Nelson, C., Max, E., 1991. Lda measurements of velocities and turbulence in a bluff body stabilized flame, in: *Laser Anemometry* 3, ASME.
- [43] Smagorinsky, J.S., 1963. General circulation experiments with primitive equations. *Mon. Weather Rev.* 91(3), 99–164.
- [44] Tatsuno, M., Takayama, T., Amamoto, H., Ishi-i, K., 1990. On the stable posture of a triangular or a square cylinder about its central axis in a uniform flow. *Fluid Dynamics Research* 6, 201–207.

- [45] Thom, A., 1933. The flow past circular cylinders at low speeds. Proc. R. Soc. Lond. A141, 651–669.
- [46] Trias, F.X., Gorobets, A., Oliva, A., 2015. Turbulent flow around a square cylinder at Reynolds number 22,000: A DNS study. Comput. Fluids 123, 87–98.
- [47] Tsuji, Y., 1999. Peak position of dissipation spectrum in turbulent boundary layers. Physical Review E 59(6), 1464–1471.
- [48] Vandoormaal, J.P., Raithby, G.D., 1984. Enhancements of the SIMPLE method for predicting incompressible fluid flows. Numer. Heat Transfer 7, 147–163.
- [49] Vreman, A.W., 2004. An eddy-viscosity subgrid-scale model for turbulent shear flow: Algebraic theory and applications. Phys. Fluids 16(10), 3670–3681.
- [50] Welch, P., 1967. The use of fast fourier transform for the estimation of power spectra: a method based on time averaging over short, modified periodograms. IEEE Trans. Audio Electroacoust. 15(6), 70–73.
- [51] Weller, H.G., Tabor, G., H., J., Fureby, C., 1998. A tensorial approach to computational continuum mechanics using object-oriented techniques. Comp. Phys. 12(6), 620–631.
- [52] Williamson, C.H.K., Wu, J., Sheridan, J., 1995. Scaling of streamwise vortices in wakes. Physics Fluids 7(10), 2307–2309.
- [53] Yagmur, S., Dogan, S., Aksoy, M.H., Goktepe, I., Ozgoren, M., 2017. Comparison of flow characteristics around an equilateral triangular cylinder via PIV and Large Eddy Simulation methods. Flow Meas. Instrument 55, 23–36.
- [54] Yeung, W.W.H., Parkinson, G.V., 2000. Base pressure prediction in bluff-body potential-flow models. J. Fluid Mech. 423, 381–394.
- [55] Yoshizawa, A., 1986. Statistical theory for compressible shear flows, with the application to subgrid modelling. Phys. Fluids 29(2152), 1416–1429.
- [56] Zahiri, A.P., Roohi, E., 2019. Anisotropic minimum-dissipation (AMD) subgrid-scale model implemented in OpenFOAM: Verification and assessment in single-phase and multi-phase flows. Comput. Fluids 180, 190–205.
- [57] Zheng, Y., Fujimoto, S., Rinoshika, A., 2016. Combining wavelet transform and POD to analyze wake flow. J. Visualization 19, 193–210.